Interactions of Steep-Fronted Pressure Waves with a Heterogeneous Combustion Field

Hans. G. Ruppik*
DFVLR-Institut für Chemische Antriebe und Verfahrenstechnik (ICAV), Federal Republic of Germany

Pressure-time-position relations and the simultaneous determination of other important combustion parameters have been theoretically and experimentally performed. These results were generated along a rocket combustor axis during propagation of a strong shock wave running back and forth through an heterogeneous combustion field and reflecting at the combustor ends. The initial steady-state condition is recognized as being that of a liquid bipropellant droplet spray combustion within the burner, limited by their simultaneous vaporization. Substantial interaction effects between the different axial distributions of mass, impulse, and energy sources, affecting the local energy release and the onset and behavior of a sawtooth-like pressure wave have been investigated. In order to study the pressure-time behavior at different burner locations a short shock tube was mounted in the opposite direction to the combustion gas flow at the downstream end of the combustor. This pulse generator functions as an additional "external" source of pulse energy to initiate the upstream-running shock. Therefore a single steep-fronted pressure pulse could enter the combustor axially at any time during the run. The governing unsteady differential equations of the gaseous phase have been solved by applying the numerical Lax-Wendroff two-step procedure, including the simultaneous bipropellant vaporization and the wave reflection at the injector end of the combustor. The initial conditions, as given by solving the steady-state problem at first, were fitted to corresponding measurements of the local combustion efficiency. This paper compares some of the recently achieved theoretical results with the corresponding experiments.

Nomenclature

A = vector function with respect to time t
A = area
a = sound velocity
B = vector function with respect to position x
C = vector function with respect to the additive terms
c = specific energy
c_d = drag coefficient
c^* = characteristic velocity
D = diameter
e = specific internal energy; exponential function
F = drag force per volume unit
f = drag force per droplet element
H = molar enthalpy
h = specific enthalpy per mass unit
i = number of position steps
IN = injector-nozzle wave travel direction
k_d = binary molecular gas diffusion coefficient
k_f = thermal conductivity coefficient
k_h = heat transfer coefficient
k_m = mass transfer coefficient
L = work per volume and time unit
M = molecular weight
m = droplet group; element number; mass of single droplet
$\dot{m}_t$ = total mass flow
N = number of droplets per second
NI = nozzle-injector wave travel direction
n = droplet group and element number
p = pressure
Q = heat flow per second
q = specific heat flow per volume and time unit
R = universal gas constant
r = oxidizer to fuel mass ratio
T = temperature
t = time
u = gas velocity
v = droplet velocity
X = mass fraction
x = space coordinate
γ = adiabatic exponent
Δ = difference
ρ = density
ϕ = mass per time and volume unit
ζ = vaporization efficiency

Subscripts

c = chamber
d = droplet; drag; diffusion
f = formation state; fuel
g = gaseous state
h = heat
i = injection state; space variable; number of components
j = droplet group number; time variable; component of the final mixture
l = liquid state
m = maximum
o = steady-state
ox = oxidizer
p = at given pressure
T = at given temperature
t = partial differentiation with respect to time; total
th = throat; theoretical
v = vaporization state
x = partial differentiation with respect to position

Superscripts

$\bar{(\ )}$ = averaged value
$(\ )'$ = per time unit

Received June 10, 1977; revision received Nov. 15, 1977.

Index categories: Shock Waves and Detonations; Combustion Stability, Ignition, and Detonation; Combustion and Combustor Designs.

*Research Scientist.

Introduction

THE appearance of steep-fronted wave phenomena which spontaneously occur during liquid-propellant rocket motor runs has long been observed by some investigators. For the first time Berman[1] and Ellis[2] observed the development of such shock-like waves from sinusoidal wave forms. Crocco

et al.[3] later found, that such discontinuous wave forms can appear in a rocket motor performance map within well-known ranges of acoustical combustion chamber instabilities. Morgan et al.[4] confirmed these results with a 44 kN liquid-hydrogen/liquid-oxygen bipropellant research motor. These phenomena can be found within particular "pulse sensitive" limits as investigated, for example, in Ref. 5. They can be triggered instantaneously, not only by an abrupt starting or hypergolic ignition process, but also very often by the onset of a single finite-amplitude disturbance during steady-state heterogeneous combustion.

Agosta et al.[6] have already recognized and described a few of these phenomena which occur during triggering and propagating axial-oriented pressure waves. Since their measuring systems were partially insufficient at that time, their results and statements were finally restricted to being more qualitative. For the first time Bracco[7] was able to experimentally describe the propagation of an external axially-initiated shock through the combustion chamber before the initial shock was reflected from the injector plane. Unfortunately his results are based on only a few experiments conducted with a LOX/kerosene research combustion tube.

Systematic experimental investigations have therefore been performed, in order to better understand the occurance of steep-fronted pressure waves. Particularly, measurements of the *p-t-p* behavior was of primary concern, depending on the local properties of an heterogeneous liquid-propellant combustion field.[5]

A research combustor with a variable-length radial nozzle was mounted at the downstream end with a short shock tube directed opposite to the flow of the combustion gas. Therefore a single shock could enter the combustion chamber at any time during the run. Simultaneous transition pressure measurements with extremely high time resolution were performed at numerous axial locations within the steady-state flows in front of the shock and also during its propagation.[5,8] Figure 9 shows the experimental apparatus. The experimental results were compared with the predictions of an unsteady computer model which is more thoroughly described in the following sections.

The Analytical Model

To describe the shock propagation through an axial heterogeneously distributed combustion field the time-dependent integration of the complete set of nonlinear partial differential equations of the gas phase must be performed along the combustor axis. Special source terms, which originate from the mass, impulse, and energy exchange between the simultaneous bipropellant droplet spray vaporization reaction and the surrounding hot-gas conditions, augment the differential equation system. These are complemented by thermochemical equations which describe the local hot-gas reaction state.

By transforming the resulting gas-phase differential equation system into the mathematical vector form, a single vector equation can be obtained

$$A_t + B(A)_x + C = 0 \tag{1}$$

Partial differentiation with respect to the time t and position x is indicated by the corresponding subscripts.

Assuming a constant area combustor, the vector components are represented by[5]

$$A = \begin{bmatrix} \rho \\ \rho u \\ \rho[(h/\gamma) + (u^2/2)] \end{bmatrix} \quad B(A) = \begin{bmatrix} \rho u \\ \rho u^2 + p \\ \rho u[h + (u^2/2)] \end{bmatrix} \quad C = - \begin{bmatrix} \Phi \\ \Phi v - F \\ \Phi[h_l + (v^2/2)] - q - L \end{bmatrix} \tag{2}$$

The inhomogeneous term C represents the mass, impulse, and energy sources, which couple the differential equations of the liquid bipropellant droplet spray.

The governing differential equations for a single liquid spherical droplet describing the time-dependent change of its diameter and velocity and also the radius-dependent change of its temperature are

$$\frac{dD}{dt} = -\frac{2}{\rho_l A_l}\frac{dm}{dt} - \frac{D}{3\rho_l}\left(\frac{d\rho_l}{dT_l}\right)\frac{dT_l}{dt} \tag{3}$$

$$\frac{dv}{dt} = \frac{3}{4} c_d \frac{\rho_g}{\rho_l}\frac{1}{D}(u-v)\,|u-v| \tag{4}$$

$$\frac{dT_l}{d(D/2)} = \frac{k_h}{\bar{k}_f}(T_g - T_l)\frac{z}{e^z - 1} - \frac{\Delta H_v}{\bar{k}_f \pi D^2}\frac{dm}{dt} \tag{5}$$

with

$$z = \frac{c_{pv}}{k_h \pi D^2}\frac{dm}{dt}$$

Calculating the molecular binary gas diffusion coefficient k_d by the equation of Bird[9] and then establishing the mass transfer coefficient of the droplet k_m by the empirical Ranz-Marshall equation[10] enables us to find dm/dt in a well-known manner. The drag coefficient c_d may also be found, e.g. by the empirical correlation functions of Rabin et al.[11] The heat-transfer coefficient k_h results from a second empirical correlation equation of Ranz-Marshall.[10] The radial temperature distribution within an evaporating spherical fuel droplet has been calculated by the application of Grossman's method.[12]

The well-known empirical correlation of Nukyama-Tanasawa has been used to define the size and mass distribution of the droplets at the spray formation point near the injector plane. Mean droplet diameters can be defined for each droplet group by assuming a mass-medium droplet diameter of the spray and dividing the total mass flow $\dot{m}_t$ into a number of arbitrarily selected parts $X_j \dot{m}_t$. These droplet diameters were initially held constant within the groups and only varied by vaporization and combustion along the x-axis of the burner. The initial droplet number per unit time of each droplet group was held constant, thus $N_j \neq N(x;t)_j$, whereby droplet collisions and a secondary breakup of droplets are excluded. The other initial spray droplet conditions are considered to be equal to the real injection conditions of the liquid propellants. Each drop size group represents a separate liquid phase, calculating the single droplet behavior and summing them over all droplets of each group. The fraction of chamber volume occupied by the spray is negligible. No exchange terms are considered.

Summing Eqs. (3-5) for a number of droplet spray groups at the axial chamber location x_i, the interphase coupling terms which augment the fluid dynamic equations are simply

Mass

$$\phi_i = \frac{1}{A_i}\sum_{j=1}^{n}\left(\frac{N\dot{m}}{v}\right)_j \tag{6}$$

with

$$N_j = \frac{6}{\pi}\left(\frac{X}{d^3\rho_l}\right)_j \dot{m}_t$$

where

$$\dot{m} = \mathrm{d}m/\mathrm{d}t$$

Impulse (force resulting from the droplet frictional drag)

$$F_i = \frac{1}{A_i} \sum_{j=1}^{n} \left(\frac{N f}{v}\right)_j \tag{7}$$

with

$$f = m\frac{\mathrm{d}v}{\mathrm{d}t}$$

Energy (work per volume and time unit required for accelerating the droplets)

$$L_i = \rho \sum_{j=1}^{n} (f\,v)_j = \sum_{j=1}^{n} (F\,v)_j \tag{8}$$

Energy (heat flux per volume and time unit required for increasing the droplet temperature)

$$q_i = \frac{1}{A_i} \sum_{j=1}^{n} \left(\frac{N Q_1}{v}\right)_j \tag{9}$$

The contribution to the gas-phase energy conservation equation follows from the two equations: the enthalpy per mass unit of the gaseous reaction end-products and the initial enthalpy of the unburnt, but evaporated, propellant spray mixture, like

$$h = \left(\sum_{j=1}^{m} X_j M_j\right)^{-1} \sum_{j=1}^{m} X_j \left[\left(\frac{\Delta H_f + \Delta H_T}{RT}\right)_T RT\right]_j \tag{10}$$

and

$$h_0 = \left[\left(h_1 + \frac{v^2}{2}\right) - \left(h + \frac{u^2}{2}\right)\right] = -\frac{1}{A\,M_i \Phi}\left[\left(\Delta H_v + \int_{T_v}^{298} c_p \mathrm{d}T\right)_i \sum_{j=1}^{m} \left(\frac{\dot{m}\,N}{v}\right)_j + \left(\Delta H_v + \int_{T_v}^{298} c_p \mathrm{d}T\right)_i \sum_{j=m+1}^{n} \left(\frac{\dot{m}\,N}{v}\right)_j\right] \tag{11}$$

where $i = 1, 2$ the number of propellant components; $j = 1, 2, \ldots, m$ and $j = (m+1), \ldots n$ the number of droplet groups of each propellant component.

The hot-gas composition can be found from the elementary reaction equations at chemical equilibrium which represent a sufficient approximation of the reaction process. The gas-phase differential equation system was completed by the global equation of state, which applies to ideal gases; i.e., when $h = h(T,\rho,X_i)$, $e = e(T,\rho,X_i)$, and $p = p(T,\rho,X_i)$

$$p = \rho R T \sum_{i=1}^{m} \left(\frac{X}{M}\right)_i \tag{12}$$

where $i = 1, 2, \ldots m$ represents the number of chemical species.

The numerical solution of the differential equation system for practical cases also requires numerous functions of properties over the widely variable conditions of pressure, temperature, and mixture ratio of the gaseous and liquid components. Tables of properties were therefore calculated by separate computer programs. A portion of these results were approximated by polynomial functions and another part of these tables was directly stored for use by the mean programs. Double spline functions were then used to find the required intermediate values between the calculated grid points.

Method of Solution

Although the most exact and convenient method of solution is to integrate the partial differential equation (1) directly along suitable characteristic directions, e.g., in the x-t plane, it is preferable to use a numerical difference procedure with fixed space and time steps. This procedure is more advantageous because the conditions for starting the unsteady problem can be obtained from steady-state calculations with fixed equidistant coordinate steps. The method reported herein is the two-step Lax-Wendroff procedure as modified and comprehensively tested by Rubin and Burstein[13] for the step-wise integration of the Navier-Stokes equations.

This approximate "numerical" two-step method is based on the generation of initial time-dependent solutions using a difference scheme exact to the first order. These are expanded by a second-order difference step in which the results of the first step have been introduced.[14] The orthogonal network is defined in the x-t plane where $t \geq 0$ and $x \geq 0$. An arrangement of points distributed in the x-t lattice is denoted by $x_i = i\Delta x$, $t_j = j\Delta t$, where $i,j = 0,1,2,\ldots n$ or $i = n, (n-1), \ldots 0$. The vector $\boldsymbol{A}_{i,j} = \boldsymbol{A}(i\Delta x, t)$ is defined as the mesh function to allow thereby an approximation to the exact solution of Eq. (1). This follows from expansion in Taylor-series up to the second order with respect to time. The t-derivatives are replaced by x-derivatives, which are approximated by difference quotients. The first step can finally be written as

$$\bar{\boldsymbol{A}}_{\substack{i+1/2 \\ j+1}} = \frac{\boldsymbol{A}_{i+1,j} + \boldsymbol{A}_{i,j}}{2} + \frac{\Delta t}{\Delta x}(\boldsymbol{B}_{i+1,j} - \boldsymbol{B}_{i,j}) + \frac{\Delta t}{2}(\boldsymbol{C}_{i+1,j} + \boldsymbol{C}_{i,j}) \tag{13}$$

and the second step as

$$\boldsymbol{A}_{i,j+1} = \boldsymbol{A}_{i,j} + \frac{\Delta t}{2\Delta x}\left(\frac{\boldsymbol{B}_{i+1,j} - \boldsymbol{B}_{i-1,j}}{2} + \boldsymbol{B}_{i+1/2,j+1} - \boldsymbol{B}_{i-1/2,j+1}\right) + \Delta t \boldsymbol{C}_{i,j} \tag{14}$$

The step-wise integration of Eq. (1), using the Lax-Wendroff difference Eqs. (13) and (14) for a fixed space and time interval must satisfy the so-called Courant-Lewy stability condition[15]

$$\frac{\Delta t}{\Delta x} < \frac{1}{|u| + a} \qquad (\boldsymbol{C} = 0) \tag{15}$$

It is required for convergence in the sense of the linear stability theory in order to avoid numerical instabilities.

The steady-state equation system, which can be found from Eq. (1), must be solved previously at equidistant points along the x-coordinate to determine initial values of the matrices $\boldsymbol{A}$, $\boldsymbol{B}$, and $\boldsymbol{C}$. This defines the conditions in front of a steep, axially-propagating compression shock. Results of such steady-state calculations are represented in Fig. 1 as compared with experimental results on the basis of c^*-efficiency. This means the mass fraction of droplets evaporated in the axial distance downstream of the injector plane, divided by the total mass flow times the ratio of the local $c^* = c^*(p; m_{0x}/m_f)$ to the final theoretical c^*. A description of the method and the extensive application to the liquid-hydrogen/liquid-oxygen system can be found in Ref. 5. Corresponding to unsteady experimental results, a sawtooth-like pressure wave profile was assumed at the nozzle end of the combustor. Assuming $p(x_m; t > t_2) = p(x_m; 0)$ and $t_0 = 0$, with t_1 and $t_2 > 0$ one can simply write: $p(x_m;t) = p(x_m;0) + [p(x_m;t_1) - p(x_m;0)]\, j\Delta t/t_1$, if $j\Delta t \leq t_1$; and $p(x_m;t) = p(x_m;0) + [p(x_m;0) - (x_m;t_1)]\,(j\Delta t - t_1)/(t_2 - t_1)$, if $j\Delta t > t_1$. This defines the initial condition for the upstream-running compression shock. The other parameters of the initial shock are calculated with the Rankine-Hugoniot shock relations. The progress of the incoming initial shock produce a disturbance in the steady-state propellant-evaporation process and therefore, also in the vector $\boldsymbol{C}$ to start a new time cycle. These can be defined by the requirement that the axial shock velocity and

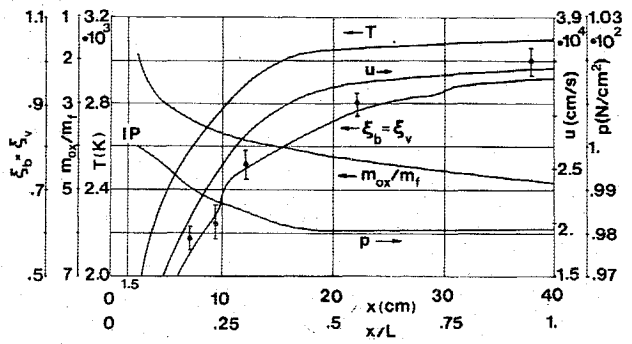

Fig. 1 Calculated steady-state hot-gas profiles, including a comparison between the calculated and the experimental local evaporation efficiency where $p_c = 10$ bar, $m_{iox}/m_f = 5$, $A_{iox}/A_{if} = 1.81$, and $A_c/A_t = 2.76$.

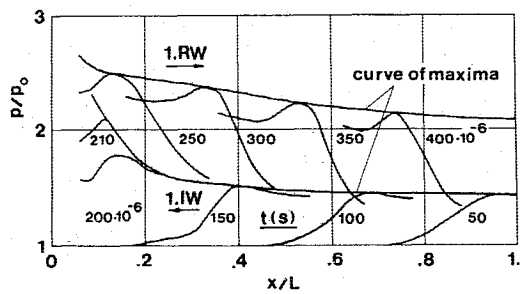

Fig. 2 *p-t-p* relation during back-and-forth wave propagation through the combustor.

also the gas velocity are zero at a plane rigid wall. It is further assumed that the x-derivative of u is constant near the wall. Neglecting any source terms at this point, the derivatives of gas pressure and density vanish, which allows the familar form of the relations $p_+ = p_-$, $\rho_+ = \rho_-$, $u_+ = -u_-$ to be applied. The subscript "+" denotes image points and the subscript "−" the corresponding interior points using $x_+ = x_- - 2\Delta x$.

Theoretical Results

Numerical solutions corresponding to the conditions of the accompanying experiments have been obtained which describe the time-dependent shock wave propagations back and forth through the heterogeneous combustion chamber flow. In the x-t plane the calculations have been predominately performed with a time step of 2 μs to avoid numerical instabilities and with equidistant x-position steps of nearly 1 cm, which were identical to the input steady-state calculations. Six characteristic droplet groups, three for the fuel and three for the oxidizer, were divided according to diameter, velocity, temperature, and concentration to represent the total mass flow. For the fuel $D_{if} = 60$, 120, 180 μ; $v_{if} = 1.92 \cdot 10^4$ cm/s; $T_{if} = 20.4$ K; and $X_{if} = 0.3$, 0.4, 0.3; and for the oxidizer $D_{iox} = 45$, 90, 135 μ; $v_{iox} = 2.4 \cdot 10^3$ cm/s; $T_{iox} = 90.2$ K; and $X_{iox} = 0.3$, 0.4, 0.3 have been used to describe the droplet groups at the initial state. The theoretical results presented in this chapter have been performed with the following combustor input data: $p_c = 10$ bar, $A_c/A_t = 2$, 74, $L_c = 41$ cm, $A_{i0}/A_{if} = 1$, 81. The unsteady calculations were obtained with a sawtooth-like shock of 40 μs pressure-rise time, a pressure ratio of 1, 4, and an assumption of a 500 μs expansion-wave duration. The results of the steady-state solution give the axial distributions of the source terms and, therefore, the local flow conditions in front of the shock wave.

Typical pressure-wave property variations during the first oscillation cycle are presented in Fig. 2 as a function of distance from the injector plane for discrete time steps. These

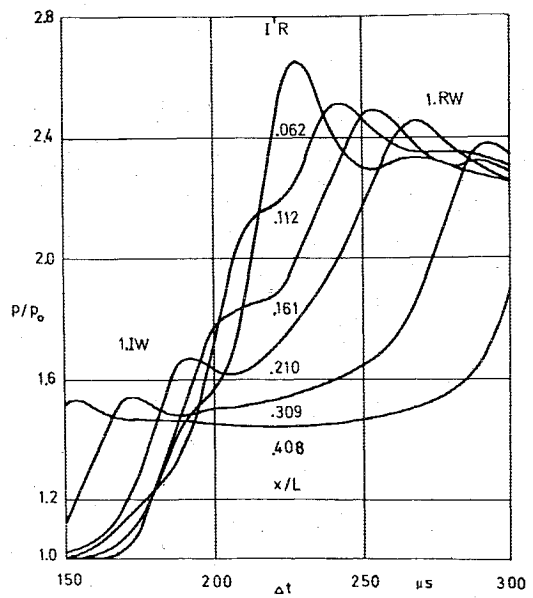

Fig. 3 *p-t-p* relation during shock reflection near the injector.

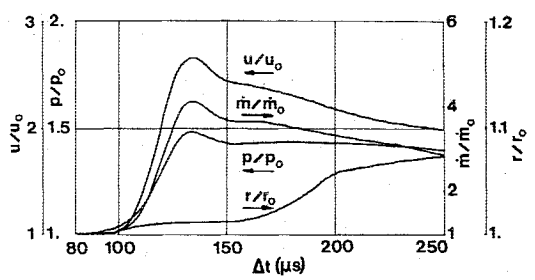

Fig. 4 Properties of the incident upstream running wave at $x/L = 0.5$.

plots are essentially "snapshots" of the various properties in the flowfield taken at specified instants of time. If the incident shock front approaches the vaporization-combustion region near the injector, one can see that large property gradients occur. As it moves through the propellant conversion regime, the front amplitude and the wavefront steepness drastically increase, indicating the effect of the local mass, impulse, and energy sources on the gas flowfield. The unsteady nature of the shock reflection is shown as a function of time in Fig. 3 at different axial locations near the injector. The pressure rise occurs continuously nearest the injector plane at the same time that the particle velocity vector decreases to zero and changes to the opposite direction. Computer results show, in addition, that the density, temperature, and oxidizer/fuel mixture ratio also increase, while the local mass flow decreases as a result of the initially decreasing droplet vaporization rate, effected by the low-velocity difference between the gaseous and liquid phases. The maximum pressure profile shows that the highest values exist near the injector end and continuously decrease in the downstream direction, depending on the local conditions in the combustion field. During the first cycle an important pressure gain can be found which drives the following oscillation cycles. Time-dependent profiles of the most important flowfield properties are shown in Figs. 4 and 5 during the time between the incident and the reflected wave passage through the middle of the chamber. One can see that the temperature profile of the upstream-running wave follows about 200 μs behind the pressure-wave profile. Therefore it passes at approximately the same time and distance from the injector as the reflected pressure wave and this possibly causes the secondary pressure wavelet in the rear region of the reflected wave.

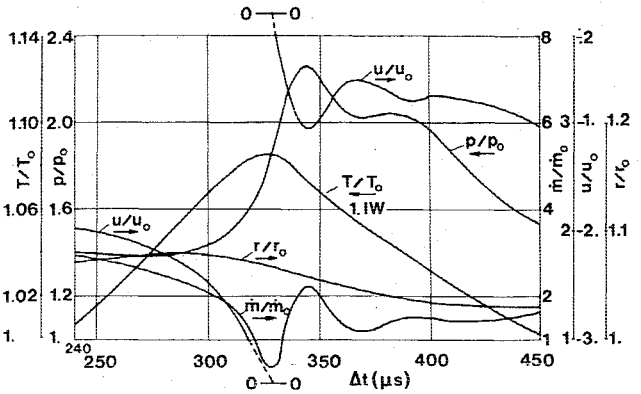

Fig. 5 Properties of the reflected wave at $x/L = 0.5$; temperature profile from the incident wave.

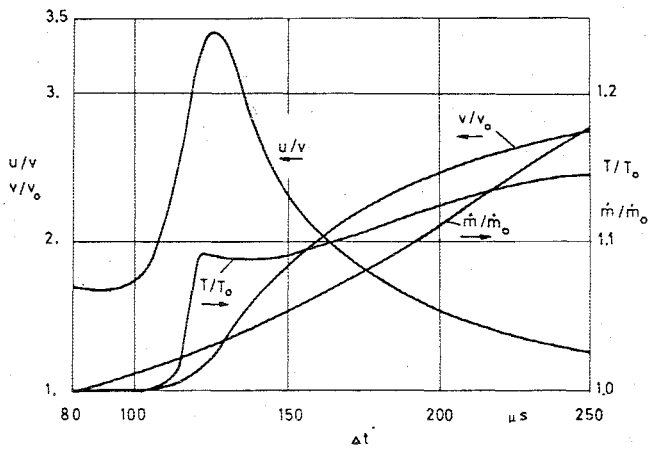

Fig. 6 Unsteady liquid droplet properties during incident wave passage at $x/L = 0.5$; oxidizer droplet diameter $D = 135\ \mu$.

Any interpretation of the temperature effect has to include the unsteady behavior of the droplet spray as shown in Fig. 6, given as an example of a single large oxidizer droplet at the same hot-gas conditions. The pressure-rise front simultaneously starts a shock-like heat-up period on the droplet surface due to the increased heat flux from the hot gas. At the same time, the interior of the droplet is apparently not affected in the absence of radiation and convection, because the realistic liquid-thermal conductivity limits the heat flux and concentrates the temperature gradient to the outer 10-20% of the droplet radius for large droplets.

Following a small delay the gas-liquid velocity ratio reaches a maximum. The droplets first accelerate and then decelerate. This can be attributed to the droplet drag which is also a function of the velocity difference. At the same time, the vaporization-combustion rate increases, and this causes the gas temperature behind the pressure wave to rise.

The time-dependent growth of the local mass flow is effected by the different increase in the vaporization rate of various fuel and oxidizer droplet groups and is presented in Fig. 7. This growth rate depends on the specific propellant properties and the different diameter of each droplet group. One can also observe a disappearance of the presented fuel groups through their total vaporization during the shock-wave passage. Figure 8 shows the effect of the increased vaporization along the chamber axis for different time increments which have elapsed since the start of the input wave at the downstream end. It is obvious that shock waves are an appropriate tool for improvement of the local combustion efficiency and the concentration of the propellant conversion region closer to the injector. This enables one to construct a shorter combustion chamber particularly for propellants with

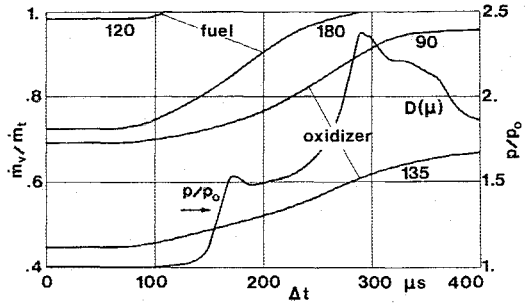

Fig. 7 Mass ratio of each single evaporated droplet group at $x/L = 0.31$ during shock transition.

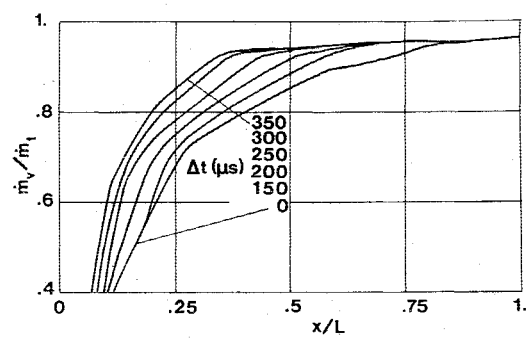

Fig. 8 Effect of the progression of the shock wave on the local hot-gas release.

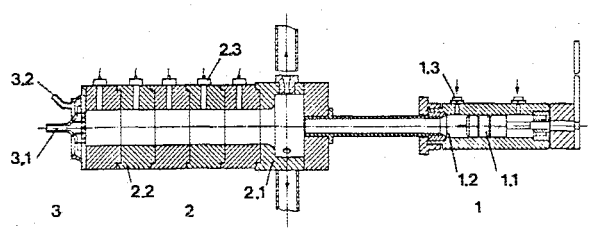

Fig. 9 *T*-burner shock tube configuration.

lower vaporization rates, assuming the wave phenomena can be sustained, e.g., by resonance effects during combustion chamber operation.

Comparison with Experiments

The object of the experiments was to determine the pressure-time relation at a number of axially distributed positions along the combustor wall, i.e. the function $p = p(x;t)$, with a high degree of time resolution. This condition was also necessary for approximating the absolute shock-wave velocity $U = U(x;t)$ and the steepness of the wave front. These quantities are dependent on the design and operating parameters of the combustor, as shown extensively in Ref. 5. A schematic view of the T-burner shock tube arrangement is shown in Fig. 9.

The calculations of the shock-wave absolute velocity were made by measuring the transit time of the pressure front between six flush-mounted pressure transducers (Kistler 603 B). Each transducer was separated by an axial distance of 5 cm, and the last one was only 2.8 cm from the injector plane. Because the transducer diaphragm diameter was nearly 0.5 cm the shock velocity uncertainty was as large as 3% for some cases.

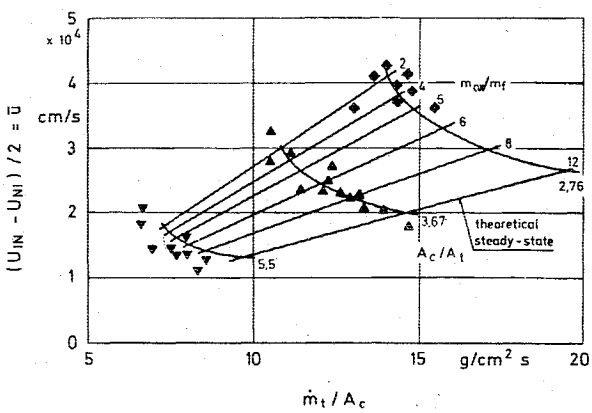

Fig. 10 Absolute shock wave velocity difference vs combustor parameters. Comparison of steady-state computer results with measurements at $x/L = 0.5$.

Figure 10 shows the difference between the downstream and upstream travelling shock velocity, measured at the same distance from the injector, versus the specific mass flow $\dot{m}/A_c$ as it depends on the propellant mixture ratios and the contraction ratios of the chamber. Dividing this difference by 2 yields the gas flow velocity if we apply the one-dimensional theory of shock propagation in ideal gases. One can see that the comparison with the steady-state theoretical solution is fairly good.

Figure 11 shows examples of a comparison between corresponding computer results and pressure profiles measured at different axial positions during the first cycle of the wave propagation. The amplitude, propagation, and steepness of the measured pressure front behave almost as predicted by the theory; the agreement seems to be substantial. The theoretical input wave conditions were selected to be identical to those generated by the shock tube during the experiments. As already shown in Fig. 1, the steady-state input calculations were fitted to separate experiments. For the purpose of quantitative research on the shock-front region, the measured analog pressure signals were stored on magnetic tape and then digitized during playback with the lowest possible tape speed. They were scanned by a data acquisition unit at 8.5 kHz and then transferred to a second magnetic tape. The results were plotted via a digital, incremental plotter using adjustable time and amplitude scales.

Figure 12 shows the nondimensional wavefront steepness during the first axial shock propagation to the injector as compared with the theory. The wavefront becomes steeper toward the injector plane, and also increases with the oxidizer/fuel mass flow ratio. As the wave moves toward the injector, a decrease in the mass ratio of combustion gas to unburnt liquid propellants will be found. Simultaneously, the unburnt oxidizer/fuel mass ratio increases which is caused by the much lower oxidizer (LOX) than fuel (LHY) evaporation rate.

Since the injection velocity of the oxidizer increases with a greater m_{ox}/m_f mass ratio, the region containing a heterogeneous mixture of propellant droplets and combustion gas extends farther downstream into the combustion chamber. This is indicated by the maximum amplitude and steepness of the wavefront, which also increases earlier. This result is possibly effected by alteration of the oxidizer jet disintegration mechanism. Thus, the droplets become larger and are formed later, due to the decreasing velocity difference between the parallel-injected propellant jets.

Conclusions

The behavior of a steep-fronted pressure wave which propagates axially back and forth through a heterogeneous, liquid bipropellant combustion field has been investigated.

A computer model has been developed which numerically solves the augmented unsteady gas conservation equations

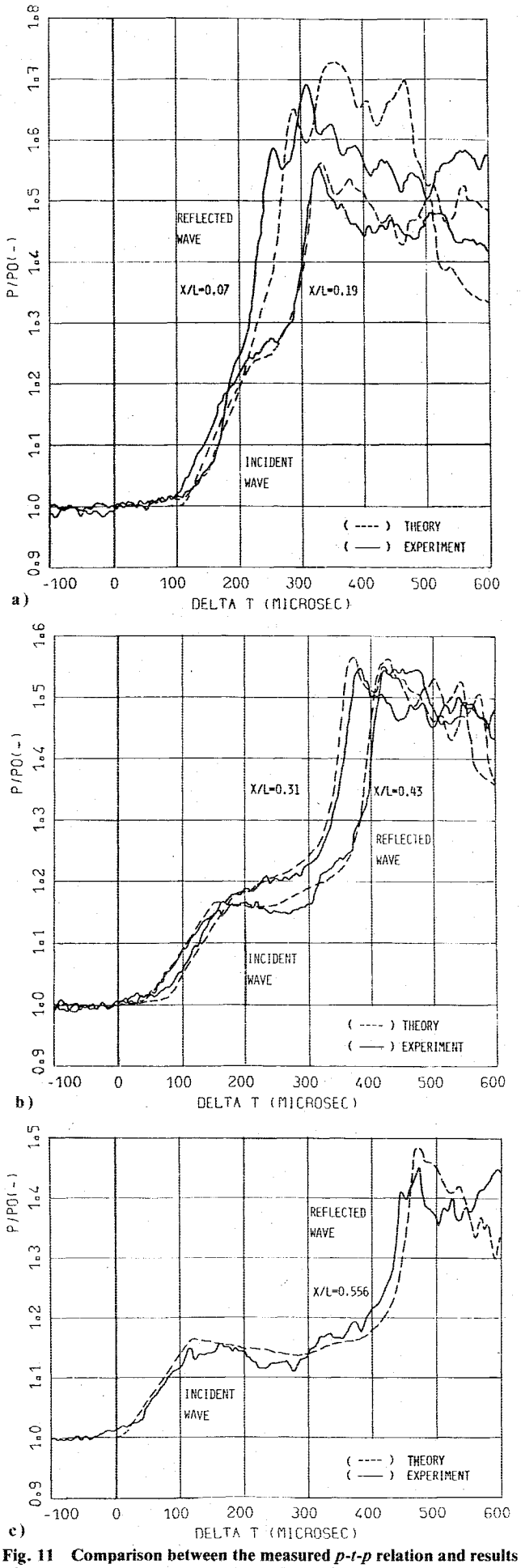

Fig. 11 Comparison between the measured *p-t-p* relation and results of the unsteady computer model at x/L = variable.

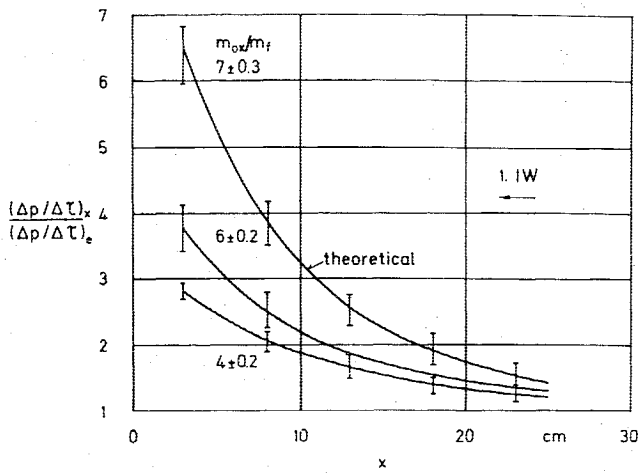

Fig. 12 Comparison of theoretical wave steepness results with experiments during the first upstream wave travel, where $A_c/A_t = 3.7$, $(\Delta p/\Delta\tau)_e = 20$ bar/ms at $x_e = 38$ cm.

including the mass, impulse, and energy addition terms from the critical evaporation of a heterogeneously distributed, bipropellant droplet field.

This procedure was applied to an upstream-running, sawtooth-like shock reflected at the injector end of a cylindrical combustion chamber. The steady-state solution of this model, which also represents the local state in front of the initial wave, was fitted by appropriate experiments. These were performed with a variable length research combustor fed with the liquid-hydrogen/liquid-oxygen propellant combination.

A short shock generator was mounted opposite the combustion gas flow as an additional "external" energy source to start a single input shock during the run. A number of minature flush-mounted pressure transducers were equally spaced along the chamber axis to measure the *p-t-p* behavior of the wave during its back and forth movement. In addition, the absolute shock velocity and the wavefront steepness have been estimated.

It can be shown that the local variations of the pressure-wave profile and the wave progress in the position-time plane occur in accordance with the equivalent theoretical results. Furthermore, one can see that the front amplitude and steepness of the incident wave drastically increase as the wave moves through the heterogeneous combustion region. This indicates the effect of the different axially distributed, mass, impulse, and energy sources within the propellant conversion zone. The maximum pressure profile shows the highest values near the injector end and continuously decreases in the downstream direction. During the first cycle an essential pressure gain can be found, which drives the ensuing oscillation cycles. The time-dependent growth of the local hot-gas mass flow which follows the shock front is affected by the varying vaporization rate increase of individual droplet groups within the propellant conversion zone. Therefore, it is obvious that shock waves are an appropriate tool for improvement of the local combustion efficiency and the concentration of the combustion zone closer to the injector.

Assuming that the wave phenomena can be sustained, e.g. by resonance effects during combustion chamber operation, one could construct a shorter liquid propellant combustor, particularly for propellants with lower vaporization rates.

References

[1] Berman, K. and Cheney, S. H. Jr., "Combustion Studies in Rocket Motors," *Journal of the American Rocket Society*, Vol. 23, 1953, p. 89.

[2] Ellis, H. et al., "Experimental Investigation of Combustion Instability in Rocket Motors," *Fourth Symposium (International) on Combustion*, 1953, p. 880.

[3] Crocco, L. et al., "Nonlinear Aspects of Combustion Instability in Liquid Propellant Rocket Motors," Princeton University, Princeton, N.J., Aeronautical Engineering Rept. 533c, 1963.

[4] Morgan, J. and Sokolowski, D. E., "Longitudinal Instability Limits with a Variable Length Hydrogen-Oxygen Combustor," NASA TN-D 6328, 1970.

[5] Ruppik, H. G., "Experimental and Theoretical Investigations on the Triggering and Propagation of Steep Fronted Pressure Waves in Liquid Propellant Rocket Engines," ESA TT-198, 1975, translation from German Rept. DLR-FB 74-67.

[6] Agosta, V. D. et al., "High Frequency Combustion Instability and Scaling of Liquid Propellant Rocket Motors," CPIA, No. 68, 1965, p. 153.

[7] Bracco, F. V., "Unsteady Mass-Energy Source Determination by a Shock Tube Technique," presented at the *Seventh JANNAF Liquid Propellant Combustion Instability Meeting*, 1970.

[8] Ruppik, H. G., "Investigation of Nonlinear Wave Phenomena in Liquid Hydrogen/Oxygen Bipropellant Rocket Engines," presented at the *Fourth Interntional Colloquium on Gasdynamics of Explosions and Reactive Systems*, San Diego, Calif., 1973.

[9] Slattery, J. C. and Bird, R. B., "Calculation of the Diffusion Coefficient of Dilute Gases and of the Self-Diffusion Coefficient of Dense Gases," *Journal of the American Institute of Chemical Engineers*, Vol. 4, No. 2, 1958, pp. 137-142.

[10] Ranz, W. E. and Marshall, W. R., "Evaporation of Drops," *Chemical Engineering Progress*, Vol. 48, No. 3, 1952, pp. 141-146 and No. 4, 173-180.

[11] Rabin, E. A. et al., "Displacement and Shattering of Propellant Droplets," AFOSR TR 60-75, 1960.

[12] Grossman, B., "Droplet Vaporization: Heat Transfer Limited Model," Master Thesis, Brooklyn Polytechnic Institute, 1965.

[13] Rubin, E. L. and Burstein, S. Z., "Difference Methods for the Inviscid and Viscous Equations of a Compressible Gas," *Journal of Computational Physics*, Vol. 2, No. 6, 1967, pp. 178-196.

[14] Richtmyer, R. D., "A Survey of Difference Methods for Non-steady Fluid Dynamics," National Center for Atmospheric Research, TN-63-2, 1963.

[15] Courant, R. and Friedrichs, K. O., *Supersonic Flow and Shock Waves*, Interscience Publishers Inc., New York, 1948.